Parameterization and Estimation of Surrogate Critical Surface Concentration in Lithium-Ion Batteries

Abstract: In this paper a surrogate electrochemical lithium-ion battery model, presented and discussed in (Di Domenico et al. - CCA, 2008) and (Di Domenico et al. - JDSMC, 2008), is parameterized and validated through experimental data by a 10 cell 37 V 6.8 Ah li-ion battery pack. Following past results (Zhang et al., 2000; Smith, 2010), the model is based on an approximate relationship between the electrode-averaged Butler-Volmer current and the solid-electrolyte interface concentration of a surrogate single particle for each cell electrode. Equally-spaced radially-discretized diffusion dynamics of the surrogate single particle for the positive electrode are then used to emulate the lithium concentration evolution in the cell. The surface concentration of the surrogate single particle, defined as surrogate Critical Surface Concentration (sCSC) is then used to predict the cell terminal voltage. The resulting model is as compact as an equivalent-circuit model but its underpinnings are lumped lithium-ion diffusion dynamics. A few parameters of the lumped lithium concentration dynamics are tuned using an iterative optimization procedure with continuous and pulsed current profiles. The single particle lithium concentration profile and the surface concentration are then estimated using a 4th order Extended Kalman Filter (EKF) and the voltage predictions are compared with data.

Keywords: Lithium-ion Battery; State of Charge; Kalman Filter.

1 Introduction

Lithium-ion batteries play an important role in the area of the second generation Hybrid Electric Vehicles (HEV) design as high-rate transient power source or in electronic devices where battery is the primary energy source. When the batteries operate in a relative limited and controlled range of state of charge, high efficiency, slow aging and no damaging are expected. As a consequence, the estimation of the State Of Charge (SOC), the power availability, and the remaining capacity are critical tasks for the battery management.

It is important to note that the SOC cannot be directly measured and the SOC definition itself varies among different works, in accordance with different points of view or different conventions. This is due not only to the instrinsic difficulty of the estimation but also to the high number of parameters and operating conditions from which the remaining charge depends. This is clear by simply looking at the discharge curves provided in the cell data−sheet by battery manufacturers, where it is possible to see how different discharge rates give different amount of energy in terms of maximum disposable amperehours.

Report Documentation Page

Form Approved
OMB No. 0704-0188

1. REPORT DATE	2. REPORT TYPE	3. DATES COVERED
01 MAR 2011	**N/A**	**-**

4. TITLE AND SUBTITLE	5a. CONTRACT NUMBER
Parameterization and Estimation of Surrogate Critical Surface Concentration in Lithium-Ion Batteries (PREPRINT)	**W56HZV-04-2-0001**
	5b. GRANT NUMBER
	5c. PROGRAM ELEMENT NUMBER
6. AUTHOR(S)	5d. PROJECT NUMBER
C. Speltion; A. G. Stefanopoulou; G. Fiengo	5e. TASK NUMBER
	5f. WORK UNIT NUMBER
7. PERFORMING ORGANIZATION NAME(S) AND ADDRESS(ES)	8. PERFORMING ORGANIZATION REPORT NUMBER
Universita degli Studi del Sannio Benevento, 82100 Italy **University of Michigan Ann Arbor, MI 48109, USA**	
9. SPONSORING/MONITORING AGENCY NAME(S) AND ADDRESS(ES)	10. SPONSOR/MONITOR'S ACRONYM(S)
US Army RDECOM-TARDEC 6501 E 11 Mile Rd Warren, MI 48397-5000, USA	**TACOM/TARDEC/RDECOM**
	11. SPONSOR/MONITOR'S REPORT NUMBER(S) **21556**

12. DISTRIBUTION/AVAILABILITY STATEMENT
Approved for public release, distribution unlimited

13. SUPPLEMENTARY NOTES
Submitted for publication in a Special Issue of Int'l Journal of Vehicle Design, The original document contains color images.

14. ABSTRACT

15. SUBJECT TERMS

16. SECURITY CLASSIFICATION OF:			17. LIMITATION OF ABSTRACT	18. NUMBER OF PAGES	19a. NAME OF RESPONSIBLE PERSON
a. REPORT	b. ABSTRACT	c. THIS PAGE			
unclassified	**unclassified**	**unclassified**	**SAR**	**28**	

Several techniques have been proposed for SOC estimation, like model-based observers (Barbarisi et al., 2006; Plett, 2004; Codeca et al., 2008; Smith et al. - CCA, 2008; Smith et al. - TCST, 2010) or black-box methods (Salkind et al., 1999) or stochastic approaches (Chiasserini et al., 2000). To our knowledge, most of the model-based observers, which have been experimentally verified, are based on equivalent circuit models. The overall voltage prediction accuracy reached is about 2% (Pop et al. - JES, 2006; Plett, 2004). SOC estimation based on electrochemical models is investigated in (Smith et al. - CCA, 2008; Doyle et al., 1993; De Vidts et al., 1995; Weidner et al., 1994), although its validation is typicaly performed against a more detailed model rather than experimental data. The electrochemical models are generally preferred to equivalent circuit representation (Chen et al., 2006), or to other kinds of simplified models, thanks to their ability to relate to the physical parameters and state limitations, whenever the battery suffers very often the stress of very high transient loads such as in automotive applications (Smith et al. - JPS, 2006). Unfortunately, electrochemical model are of high order and too complex to be tuned or used in a real-time on-board estimator. As a consequence several approximations are typically introduced (Barbarisi et al., 2006; Paxton et al., 1997; Smith et al. - JDSMC, 2008).

The aim of this paper is to validate the current/voltage behavior of a previously discussed model (see (Di Domenico et al. - CCA, 2008) and (Di Domenico et al. - JDSMC, 2008)), versus experimental data collected from a 6.8 Ah, 10 cells li-ion battery pack and show the performance of the model based Extended Kalman Filter (EKF) in voltage prediction based on solid critical surface concentration (CSC) values. While generally the standard SOC represents the battery remaining energy, the estimated CSC value represents the amount of energy that is available in the battery to be used instantaneously. This value converges to the classic SOC estimation after a rest, so it is useful even as standard charge indicator. The model is based on an approximated relationship between (i) the Butler-Volmer current and the solid concentration at the interface with the electrolyte and (ii) the battery current and voltage. In this work, the procedure used to identify the averaged model parameters in order to match the model output with the experimental data is shown in detail. The tuned model is then validated using additional battery voltage and current measurements during both charge and discharge experiments. Finally the EKF parameters are adjusted in order to estimate the battery averaged solid surface concentration and, as consequence, the battery CSC. The paper is organized as follows. First, the electrochemical model is briefly described. Then the experimental set-up and the battery parameters identification procedure are illustrated. Finally the EKF features and CSC estimation are presented along with a robustness analysis.

2 Electrochemical battery model

The lithium-ion battery is composed of three main parts: the negative electrode, the separator and the positive electrode. Each battery electrode consists of a solid matrix of porous material filled with lithium ions, immersed inside an electrolyte solution, whereas the separator is just the electrolyte solution that acts as an electronic insulator, conducting only the lithium ions. In particular,

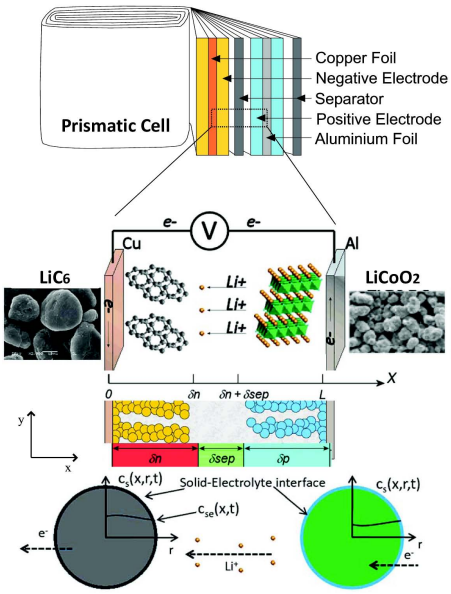

Figure 1 The battery electrodes typically extend for meters in order to have the largest possible collector area but are wound forming the prismatic or puch cells (upper). Schematic representation of the electrode thickness across the x-dimension and the surrogate single particle approximation (bottom).

the negative electrode, or anode, is generally composed of a mixture of carbon (i.e. LiC_6), while the electrolyte is a lithium salt in an organic solvent, such as $LiPF_6$ in a solution of EC:DMC. The positive electrode, or cathode, is a lithium-metal oxide and its composition can vary through different chemistries (i.e. $LiCoO_2$ or $LiMn_2O_4$) with different properties in terms of energy density, peak power, maximum discharge current or temperature rating. Batteries are generally composed from two long stripes of metallic collectors, coated with the respective active materials and wetted with the electrolyte solution. Between the electrodes, is present a special separator membrane that acts like a surge switch, preventing internal short, caused by the formation of dendrites in the collectors due to chemical reaction occurring when high (or conversely low) concentrations of lithium ions arise into the electrodes. The presence of this membrane offer a small but not irrelevant resistance. Figure 1 shows a section of the battery film across the electrodes. The green spheres represent the lithium particles trapped into the active material of anode or cathode, with the respective thickness and the length between the metallic collectors. Under the presence of a load current, the particles of lithium trapped into the solid active material at the negative electrode start to diffuse toward the electrolyte-solid interface where a chemical reaction occurs (oxidation), splitting lithium in ions and electrons. The potential difference causes the transferring of the lithium ions through the solution while the electrons are forced to move through the collector because, as said before, the electrolyte solution acts like an electronic insulator (Smith et al. - JPS, 2006). The traveling lithium ions arrived at the interface with solid material in the cathode react

again with the electrons coming from positive collector and, thanks to the inverse chemical reaction (reduction), intercalating into the metal oxide solid material as new lithium particles. The whole phenomenon is commonly called *rocking-chair*, as the lithium material flows back and forth through the battery (Tarascon et al., 1991), ideally in a fully reversible process. The lithium transportation and intercalation/diffusion process are the main aspects covered into the battery mathematical model.

It's generally accepted that a microscopic description of the battery is intractable, due to the complexity of the phenomena at the interfaces (Wang et al. - Part 1, 1998). So, in order to mathematically model the battery, both macroscopic and microscopic modeling approximations have to be considered.

Focusing in the galvanostatic operation, the input of the model is the battery current I, with positive value during discharge, while the output is the battery voltage V. The battery system assuming dominant or limiting solid-diffusion phenomena can be described with three quantities, i.e. solid concentrations (c_s) and solid and electrolyte potentials (ϕ_s, ϕ_e) (see (Smith et al. - JPS, 2006; Gu et al., 2000)) as function of the Butler-Volmer reaction current density j^{Li} describing the current distribution along the cell length.

$$\frac{\partial}{\partial x}\left(\kappa^{eff}\overrightarrow{\nabla}_x\phi_e + \kappa_D^{eff}\overrightarrow{\nabla}_x \ln c_e\right) = -j^{Li} \tag{1}$$

$$\frac{\partial}{\partial x}\left(\sigma^{eff}\overrightarrow{\nabla}_x\phi_s\right) = j^{Li} \tag{2}$$

$$\frac{\partial c_s}{\partial t} = \overrightarrow{\nabla}_r(D_s\overrightarrow{\nabla}c_s) \tag{3}$$

with electrolyte concentrations (c_e) fixed and the current density defined as

$$\int_{\delta_n} j_n^{Li}(x)dx = \int_{\delta_p} j_p^{Li}(x)dx = \frac{I}{A}. \tag{4}$$

The equations (1) to (3) have initial conditions reflecting physical and chemical constraints or based on the input current I and are are all coupled by the Butler-Volmer current density equation

$$j^{Li}(x) = a_s j_0\left[\exp\left(\frac{\alpha_a F}{RT}\eta\right) - \exp\left(-\frac{\alpha_c F}{RT}\eta\right)\right]. \tag{5}$$

The overpotential η (i.e. the extra energy needed to force the electrode to react at a required rate or equivalently to produce the required current density) is defined as

$$\eta = \phi_s - \phi_e - U(c_{se}) \tag{6}$$

where $U(c_{se})$ is the open circuit potential (OCP), i.e. the potential at which there is no current flowing through the battery, which is function of the lithium concentration inside each electrode. It is possible to find an empirical correlation

function between the solid concentrations and the open circuit potential as will be shown later in this paper. Finally, the coefficient j_0 is calculated as

$$j_0 = k_0(c_e)^{\alpha_a}(c_{s,max} - c_{se})^{\alpha_a}(c_{se})^{\alpha_c}. \tag{7}$$

Finally, the cell potential is computed as

$$V = \phi_s(x = L) - \phi_s(x = 0) - \frac{R_f}{A}I \tag{8}$$

where R_f is the film resistance on the electrodes surface and A is the collectors area. More details on the model and its parameters can be found in (Di Domenico et al. - CCA, 2008; Smith et al. - JPS, 2006; Wang et al. - Part 2, 1998).

Note here that the electrolyte concentration c_e has been neglected because, in general, it has a small gradient even under high current transients(Smith et al. - JPS, 2006). A lumped form of the lithium-ion diffusion in the electrolyte is modeled in (Schmidt et al., 2010) although Smith et al. in (Smith et al. - TCST, 2010) report that the associated eigenvalue is in the middle of the range of eigenvalues for the solid diffusion dynamics.

To further simplify the model, the solid concentration distribution along the electrode is neglected and (4) is evaluated using an average value for the current densities. An averaged solution of (4)

$$\int_0^{\delta_{n,p}} j_{n,p}^{Li}(x)dx = \frac{I}{A} = \bar{j}_{n,p}^{Li}\delta_{n,p} \tag{9}$$

ignores the spatial dependence from the Butler-Volmer equation. Because the initial conditions for the diffusion equation (3) of each spherical particle are based on the local (x-direction) value of the current density, the first effect of the averaging procedure is the possibility of describing the diffusion sub-model with a single representative solid material particle for the anode and another one for the cathode. The second effect is that equation (2) can be neglected, because its solution is now with no physical meaning. Indeed, equation (2) represents the differential expression of the Ohm's Law. Once the J^{Li} term is no longer space varying, the differential equation reverts itself to the standard $V = RI$ form and therefore there is no more need of solving it.

Because the chemical reactions are driven by the lithium-ion concentration at the electrolyte interface (i.e. $c_{se}(x)$ value) rather than the average bulk concentration, the value of the former concentration is critical in respect to the instantaneous cell conditions and its voltage output. The surface concentration resulting from the averaging process is then called critical surface concentration $\bar{c}_{sc}$ and all the model equations will be based on this particular value. Although these simplifications result in a heavy loss of information, they can be useful in control and estimation applications as we demonstrate next. With the previous assumptions made, it is possible to find a solution for the other equations allowing the simulation of the cell model.

The partial differential equation (3), describes the solid phase concentration along the radius of the active particle, but, as said above, the macroscopic model requires only the concentration at the electrolyte interface. Because it is still in

form of a partial differential equation, in order to solve this equation using Matlab-Simulink it is convenient to express the PDE into an ordinary set of ODEs, using finite differences method along the particle radius r-dimension.

$$\frac{\partial c_s}{\partial t} = \overrightarrow{\nabla}_r (D_s \overrightarrow{\nabla} c_s) = D_s \left(\frac{\partial^2 c_s}{\partial r^2} + \frac{2\partial c_s}{r \partial r} \right) \tag{10}$$

Dividing the sphere radius in $M_r - 1$ intervals, it is possible to approximate for each interval the first and the second derivative with the finite difference, so that the PDE of a generic particle becomes

$$\frac{dc_{sq}}{dt} = \frac{D_s}{\Delta_r^2} \left[c_{s_{(q+1)}} + + c_{s_{(q-1)}} - 2c_{s_q} \right] + \left[\frac{\Delta_r}{2r_q} \left(c_{s_{(q+1)}} - c_{s_{(q-1)}} \right) \right] \tag{11}$$

where $q = 1, ..., M_r - 1$ and $r_q = q\Delta_r$. Substituting r_q in (11)

$$\frac{dc_{s_q}}{dt} = \frac{D_s}{\Delta_r^2} \left[\left(\frac{q-1}{q} \right) c_{s_{(q-1)}} - 2c_{s_q} + \left(\frac{q+1}{q} \right) c_{s_{(q+1)}} \right]. \tag{12}$$

The boundary condition can be rewritten linearly, approximating center and border concentration value as follows

$$\begin{aligned} c_{s_0} &= c_{s_1}, \\ c_{s_e} &= c_{s_{(M_r-1)}} - \Delta_r \frac{j^{Li}}{Fa_s D_s} \end{aligned} \tag{13}$$

With these approximations it is possible to express the resulting $M_r - 1$ ODEs in a classic state space formulation as follows

$$\begin{aligned} \dot{c}_s &= \mathbf{A} c_s + \mathbf{B} j^{Li}. \\ c_{se} &= c_{s_{(M_r-1)}} + \mathbf{D} j^{Li} \end{aligned} \tag{14}$$

where matrices $\mathbf{A}$, $\mathbf{B}$ and $\mathbf{D}$ are

$$\begin{aligned} \mathbf{A} &= \alpha_1 \begin{bmatrix} -2 & 2 & 0 & 0 & \cdots & \cdots & 0 \\ \frac{1}{2} & -2 & \frac{3}{2} & 0 & \ddots & \ddots & \vdots \\ 0 & \frac{2}{3} & -2 & \frac{4}{3} & 0 & \ddots & \vdots \\ 0 & 0 & \ddots & \ddots & \ddots & \ddots & \vdots \\ \vdots & \vdots & \ddots & 0 & \frac{M_r-3}{M_r-2} & -2 & \frac{M_r-1}{M_r-2} \\ 0 & 0 & \dots & 0 & 0 & \frac{M_r-2}{M_r-1} & -2 \end{bmatrix}, \\ \mathbf{B} &= \alpha_2 \begin{bmatrix} 0 \\ \vdots \\ 0 \\ \frac{M_r}{M_r-1} \end{bmatrix}, \mathbf{D} = -\frac{\alpha_2}{\alpha_1} \end{aligned} \tag{15}$$

with $\alpha_1 = \frac{D_s}{\Delta_r^2}$, $\alpha_2 = \frac{1}{Fa_s D_s}$ from (12) and (13).

The number of discretization points M_r has to be chosen based on the particle size. For very small particles the diffusion phenomenon is not relevant and M_r can be chosen between $1 \div 5$. Instead, for bigger particles (i.e. with radius $r > 5$ μm) a choice of M_r between $15 \div 30$ leads to a good approximation of particle internal diffusion. In this paper we choose $M_r = 20$. Because of the second assumption made, the solutions of the single particle diffusion equations in the averaged model become respectively $c_s = \bar{c}_s$ and $c_{sc} = \bar{c}_{se}$. This solution holds both for positive and negative active materials, with the respective parameters and current density input.

Two sets of ODEs, one for the anode and one for the cathode are then obtained. The positive and negative electrode dynamical systems differ at the constant values and at the input sign. In accordance with past work it is convenient to express the concentration values in term of normalized concentration, also know as concentration stoichiometry,

$$\theta_x = \frac{c_{se,x}}{c_{se,max,x}}, \tag{16}$$

where $c_{se,max,x}$ is the maximum concentration of lithium into each electrodes and $x = p, n$ for the positive and negative electrode. Note that the concentration stoichiometry above is based on the solid-electrolyte surface lithium ion concentration, which apart from directly influencing the terminal voltage, it typically represents the extremum value of lithium concentration in the particle, hence called **critical surface concentration, (CSC)**. This definition departs from the traditional bulk concentration stoichiometry (i.e. the stoichiometry of the bulk solid concentration based on the average c_{s_i}) defined as $\theta_{b,x} = \frac{c_{b,x}}{c_{se,max,x}}$, again with $x = p, n$ for positive and negative electrode. The battery voltage (8), using (6) and using the electrode-average values at the anode and the cathode, can be rewritten as

$$V = (\bar{\eta}_p - \bar{\eta}_n) + \left(\bar{\phi}_{e,p} - \bar{\phi}_{e,n}\right) + (U_p(\theta_p) - U_n(\theta_n)) - \frac{R_f}{A} I. \tag{17}$$

Using the microscopic current average values and imposing the boundary conditions and the continuity at the interfaces, a solution of (1) can be found. As shown in (Di Domenico et al. - CCA, 2008) and (Di Domenico et al. - JDSMC, 2008), the approximate solution for the electrolyte potential difference at the interface with the collectors leads to

$$\bar{\phi}_{e,p} - \bar{\phi}_{e,n} = \phi_e(L) - \phi_e(0) = \tag{18}$$

$$= -\frac{I}{2Ak^{eff}} \left(\delta_n + 2\delta_{sep} + \delta_p\right).$$

Each of the individual voltage submodels in (17) can be expressed as a function of the surface solid concentration and the input current as following. Using (5) it is possible to express the overpotentials difference as a function of average current densities and solid concentrations as follows

$$\bar{\eta}_p - \bar{\eta}_n = \frac{RT}{\alpha_a F} \ln \frac{\xi_p + \sqrt{\xi_p^2 + 1}}{\xi_n + \sqrt{\xi_n^2 + 1}} = V_\eta(\theta_{p,n}, I) \tag{19}$$

where

$$\xi_p = \frac{\bar{j}_p^{Li}}{2a_s j_{0p}} \quad \text{and} \quad \xi_n = \frac{\bar{j}_n^{Li}}{2a_s j_{0n}}. \tag{20}$$

The battery voltage (17) can now be rewritten as a function of current demand and average solid concentration

$$V(t) = V_\eta(\theta_{p,n}, I) + (U_p(\theta_p) - U_n(\theta_n)) - \frac{K_r}{A} I. \tag{21}$$

where $K_r = \frac{1}{2\kappa^{eff}} (\delta_n + 2\delta_{sep} + \delta_p) + R_f$ is a term that takes into account both internal and collector film resistances.

3 Experimental Set-Up

The battery utilized in the experimental set-up is a 6.8 Ah polymer lithium-ion battery from SAFT composed of a series of ten MP176065 cells with a nominal pack voltage of 37 V. The battery pack is equipped with a protection circuit limiting the current demand to 5 A by an internal amperometric fuse. The experiments have been conducted with lower current demands. In order to collect the battery experimental data during the charge and the discharge, a series of electronic devices have been utilized. The experimental set-up is composed of an electronic load Prodigit-3600, a DC voltage generator and a voltage-current sensor coupled to a 16-bit ADC from National Instruments. Figure 2 shows the connection schematics between the battery, load and generator, coupled with the voltage/current sensor. The DC voltage generator utilized for the battery charge is a 42 V - 20 A device and was charging the battery according to the manufacturer specifications taking into account safety concerns and cell balancing. Finally the data has been collected using a 16-bit, 32 channels A/D converter from National Instruments that able to sample the current and voltage signals at a maximum rate of 1 MHz. The sampling time has been chosen in a range from 0.1 s to 0.025 s in order to avoid oversampling during slow rate experiments or conversely undesired aliasing during faster load dynamics.

4 Model Identification Procedure

The surrogate single particle model depends on fewer parameters with respect to the electrode-distributed one, but this number is still too high to identify all of them as unknowns. Some of the parameters capture geometrical features and some chemical features which can be split into physical and design specific (i.e depend on the particular cell design). In order to reduce the number of parameters to be identified and maintain a good degree of accuracy for model fitting, some values have been taken from literature (Smith et al. - JPS, 2006) and some from the cell manufacturer.

The parameters to identify are the maximum positive and negative solid concentration $c_{s,max,p}$ and $c_{s,max,n}$, the positive and negative solid phase diffusion

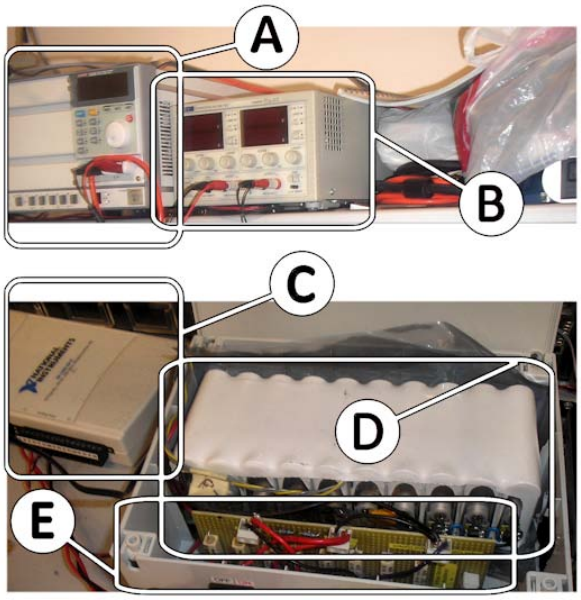

Figure 2 Experimental set-up: (A) Electronic load, (B) Voltage generator, (C) ADC, (D) Battery and (E) Current and voltage sensor.

coefficient $D_{s,p}$ and $D_{s,n}$, the positive and negative active surface area per electrode $a_{s,p}$ and $a_{s,n}$, the electrode surface A, the total cell film resistance K_r and the current coefficient k_0 for a total of **nine** parameters. In addition to these nine parameters it is necessary to know the initial solid concentration values in both electrodes. The discharge and the charge experiments have been conducted with the battery respectively fully charged and fully discharged in order to reduce the influence of an erroneous estimate of the initial concentration. An initial estimate for the fully charged stoichiometry is taken from (Doyle et al., 1993). These values have been adopted and then refined to fit the experimental data.

In order to obtain the correlation between solid concentration inside the electrodes and their open circuit potential, the following procedure has been adopted. From the battery data sheet it is possible to know that the negative electrode active material is composed of graphite (LiC6) so the empirical correlation found in (Fuller et al. - I, 1994) has been utilized, while the positive consists of an unknown mixture of LiCoO2 with other metal oxides. Since the positive OCP dominates the terminal open circuit voltage, an empirical correlation has been established for $U_p(\theta_p)$ by discharging the cell at a very low constant rate and fitting the difference between observed data and model voltage output.

Figure 3 shows the empirical correlations found for both electrodes. The other battery constants are shown in Table 2. The parameter identification procedure has been designed as follows. A set of experimental data has been chosen for the parametric identification routine, comprised of charge and discharge process, with constant and pulse current profile, in order to capture both slow and fast dynamics of the battery behavior. In detail, a set of four charges (1 A, 2 A and 3 A at constant current and 4 A with pulse current demand) and four discharges (2 A,

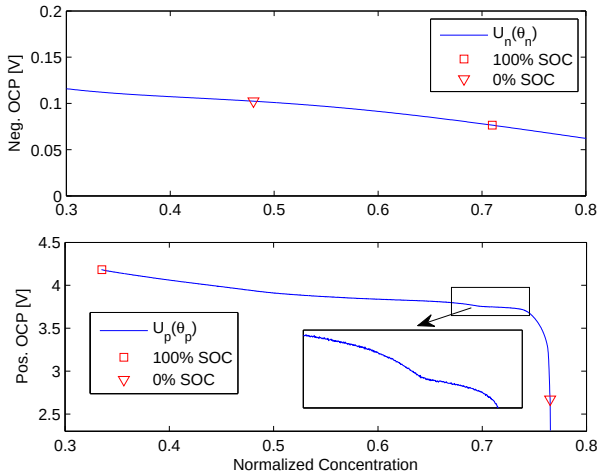

Figure 3 Empirical open circuit potential correlations for negative and positive electrodes.

3.5 A and 5 A at constant current and 6 A pulse current demand) have been utilized for parameter identification. Note here that the identification procedure on a single profile leads to a very good fit, but the obtained parameters are tied to the specific experiment and do not fit well with other experiments. In order to avoid this local minimum problems and obtain a set of parameters matching different operational points, a global identification procedure has been conducted utilizing all the selected data at the same time. The identification procedure consists of finding the minimum of the following index cost:

$$\min_{par} J = \sum_{i} \int (V_{M,i}(I_i, par) - V_{REC,i})^2 \tag{22}$$

where $V_{REC,i}$ is the *i-th* experimental battery voltage measurement recorded corresponding to the *i-th* current demand profile I_i, $V_{M,i}(I_i, par)$ is the predicted voltage and *par* is the vector of parameters to identify. In order to obtain a guess starting point for the parameter set, a rough estimation of their values has been obtained utilizing information from literature and battery nominal performance. The minimization procedure has been conducted using Matlab/Simulink, with a gradient free function minimization algorithm specifically suited for non-linear scalar function. The single experiment maximum error tolerance has been fixed around ± 0.5 V corresponding to a maximum error of ± 0.05 V per cell. In addition it is necessary to fit the Open Circuit Potential (OCP) correlation function for the positive electrode, because it is related to the specific cell properties. The OCP is the potential at which there is no current flowing into the battery. For each electrode its value can be related with the solid surface concentration through an empirical correlation function, representative of chemical, geometrical and physical properties of the electrode construction. In literature it is possible to find expression of that correlation for cathode material (LiCoO2 or LiMnO4) or anode (LiC6), but those functions appear to be fitting only for their original

battery measurements (Doyle et al., 1996; Fuller et al. - II, 1994; Doyle et al., 2003)

So, it is necessary to fit a custom correlation function for our MP176065 cells in order to reproduce the battery voltage behavior, especially for low SOC values. From battery manufacturer specification it is possible to know that the anode is composed of graphite (LiC6), while the cathode is a mixture of LiCo02 and other metal oxides. The negative OCP value is very small and slowly varying with negative solid concentration, so instead of fitting a custom function we used a correlation found in literature (Fuller et al. - I, 1994). Instead, fitting the positive OCP function is a part of the identification process.

Because the cathode material is mainly composed of LiCoO2 and in accord with data collected, the positive correlation function is expected to be similar to the one found in literature (Doyle et al., 2003), especially in the initial phase of a discharge, when positive stoichiometry is low and porous structure is more likely to accept new lithium ions insertion. For this motivation the fitting procedure has been modeled as follows:

A) - The initial parameter values for the model are taken from prior work and the positive OCP used is based on Doyle et al. formula. The identification procedure is run, using current/voltage profiles truncated before (or after during a charge) the end of discharge, as shown in Figure 4-A.

B) - The obtained OCP is compared with experimental data collected during a 0.1 C charge and discharge (i.e. 0.68 A). For such very low current demand, the battery voltage is approximately equal to the open circuit voltage as is shown in Figure 4-B. The battery specific correlation function is computed as follows:

$$\hat{U}_p = V_{OCV} - V_{MOD} + U_p^D \tag{23}$$

where $\hat{U}_p$ is the estimated OCP correlation, V_{OCV} is the collected battery open circuit voltage, V_{MOD} is the model output computed as in (21), and U_p^D is the positive OCP computed as in (Doyle et al., 2003)

C) - The newly found OCP correlation is substituted to the old one. Figure 4-C shows the new found correlation confronted with the old one.

D) - The identification procedure is run again, but without cropping the data set after the end of discharge (or conversely the beginning of charge). Figure 4-D shows an identified voltage profile with the new found OCP function.

E) - If the step D ends with a voltage error smaller than the fixed threshold (0.5 V in this case), the identification procedure ends. Otherwise start again from step A, using the identified parameter set but substituting U_p^D with the new found function in order to refine the result during step B. The minimization function is then kept running until all individual errors are under fixed threshold and the voltage profile is correctly followed by the model.

5 Simulation Results

After the identification procedure the reduced order model exhibits a good voltage prediction, with an approximate mean error of 0.2 V and a maximum error under

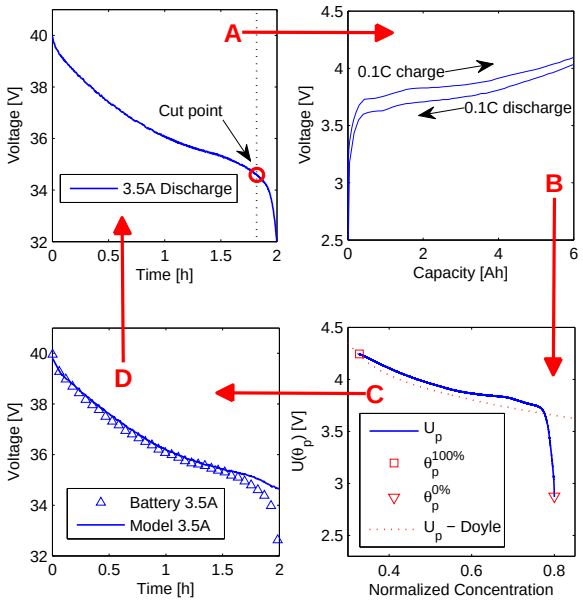

Figure 4 Open Circuit Potential identification procedure.

the chosen threshold. The resulting parameters values are listed in Table 1. Figure 5 shows the obtained voltage prediction under charge and discharge at different rates, during the model identification process. The solid lines represent the model output, while the marks represent experimental data. The simulations show a good agreement under all conditions and particularly good results away from the initiation and the termination of the experiments. During the initiation and the termination phase of its experiments, the internal battery protection circuitry is activated, hence it cause nonlinear phenomena which are not modeled.

Figure 6 shows the identification procedure results on a pulse operation discharge. For visualization reason, only the first 150 s of the simulation are shown, but results are representative of the entire test. The fast transients are followed without errors, showing good dynamic performances.

Finally the model has been validated on a different data set, not utilized for identification purpose. The current demand profile used for validation purpose is a series of ten Hybrid Pulse Power Characterization profiles (HPPC), as indicated in the FreedomCar manual (US DoE, 2003). Each HPPC profile lasts 60 s with reference current demand increases of 0.5 A (starting from 0.5 A up to 5.5 A), and is followed by 15min relaxation period. Figure 7 shows the complete simulation, while Figure 8 zoom only in a selection of the signal, in order to best illustrate the result. The battery measurement has been under sampled in order to improve readability of the figure.

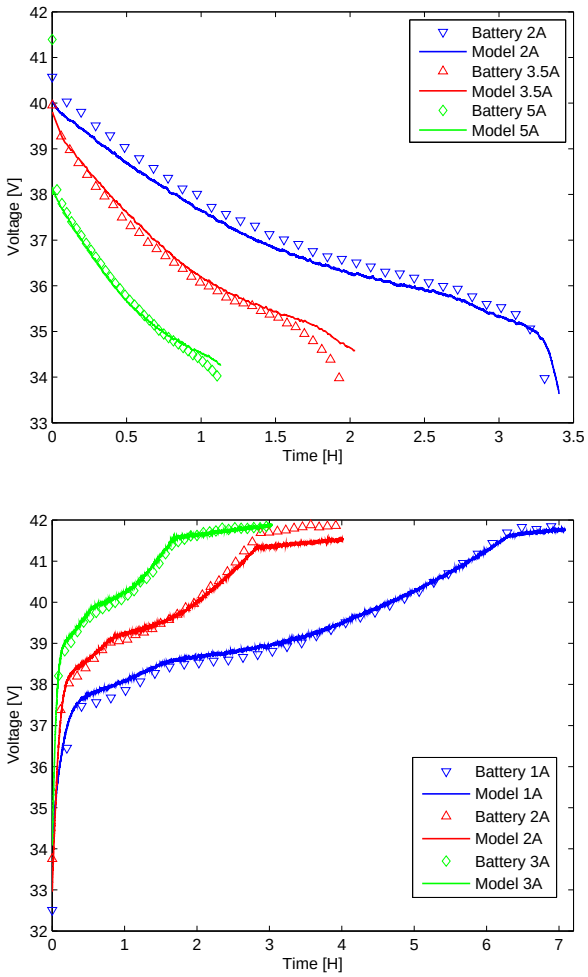

Figure 5 Battery measurement versus battery model during identification test experiment. Upper plot shows discharge experiments, while bottom plot shows charge experiments.

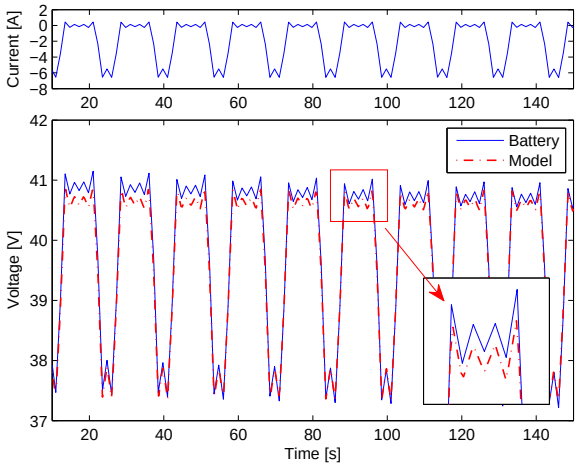

Figure 6 Battery measurement versus battery model during identification test experiment, under pulse current discharge.

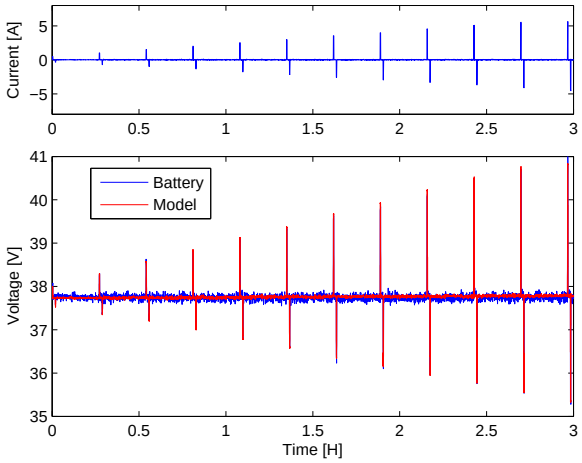

Figure 7 Battery measurement versus battery model during validation test experiment, under repeated HPPC current demand profile.

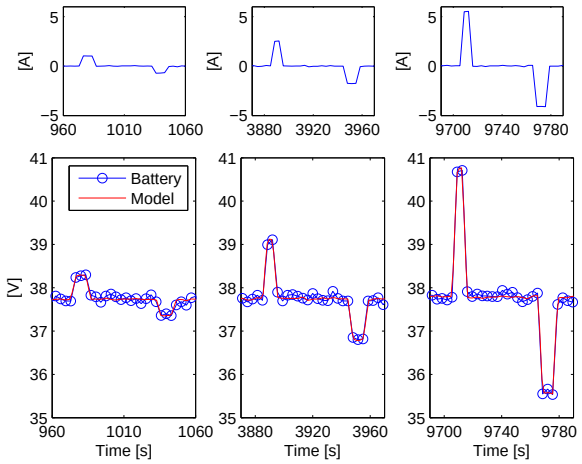

Figure 8 Detail on selections of validation test experiment.

6 Kalman filter State of Charge estimation

The physical quantity related to the battery state of charge is the solid concentration at the electrodes. A Kalman Filter for the on-line SOC estimation based on the electrochemical model is presented in (Di Domenico et al. - CCA, 2008) and (Di Domenico et al. - JDSMC, 2008), where a preliminary observability analysis is also performed.

6.1 System Observability

In order to study the system observability it is necessary to transform the model in a linear state-space formulation from the current input I through the voltage output V.

The average dynamical system (14) describes the diffusion effects into two solid material particles, one for the cathode and one for the anode, and allows to compute the solid concentration at the spheres radius, which represents an average value of the solid concentration throughout the electrodes. Defining the state vector as

$$x = (c_{s,n1}, c_{s,n2}, ..., c_{s,nM_{r-1}}, c_{s,p1}, c_{s,p2}, ..., c_{s,pM_{r-1}}) \tag{24}$$

where $c_{s,ni}$ and $c_{s,pi}$, with $i \in 1, 2, ..., M_{r-1}$, refer to the concentration values inside respectively the negative and the positive representative particles for each electrode. The linear system of the single-particle two-electrode battery is then

$$\dot{x} = Ax(t) + Bu(t) \tag{25}$$

where

$$A = \begin{pmatrix} A_n & 0 \\ 0 & A_p \end{pmatrix} \tag{26}$$

with A_n and A_p obtained from (15) using respectively anode and cathode constants,

$$B = \begin{pmatrix} B_n & 0 \\ 0 & B_p \end{pmatrix} \tag{27}$$

with B_n and B_p again from (15) and

$$u = (\bar{j}_n^{Li}, \bar{j}_p^{Li})^T. \tag{28}$$

The system matrices highlight that the electrode dynamics are decoupled due to the averaging of the current density (while in the original equation set are connected through the spatial varying potentials and the current density). The final battery voltage is then calculated as

$$y = V = f(x, u). \tag{29}$$

Because the function f is non-linear it is necessary to compute the C matrix by linearizing the output $y(t)$ around operating point $(\bar{x}, \bar{u})$ as follows

$$y \approx f(\bar{x}, \bar{u}) + \left.\frac{\partial f}{\partial x}\right|_{x=\bar{x}} (x - \bar{x}) + \left.\frac{\partial f}{\partial u}\right|_{u=\bar{u}} (u - \bar{u}) \tag{30}$$

which leads to

$$C = \left.\frac{\partial f}{\partial x}\right|_{x=\bar{x}}. \tag{31}$$

Because of the weak dependence of j_0 on the solid concentration in (7), it is possible to express

$$C = \left(0, -\frac{\partial U_n}{\partial c_{s,nM_{r-1}}}, 0, \frac{\partial U_p}{\partial c_{s,pM_{r-1}}}\right). \tag{32}$$

The observability matrix O is then obtained according to

$$O^T = [C^T (CA)^T (CA^2)^T ... (CA^{M-2})^T]. \tag{33}$$

Even if O is a full rank matrix, it has to be noted that because U_n is a weak function of $c_{se,n}$ (its derivative is almost zero) it is possible that in some operating points O is approximately singular. In addition, the voltage expression is an approximated solution of (8) and it is based on the differences between positive and negative quantities, leading to the observability of their differences more than the individual absolute electrode behavior. So the system that includes both positive and negative electrode concentration states is weakly observable.

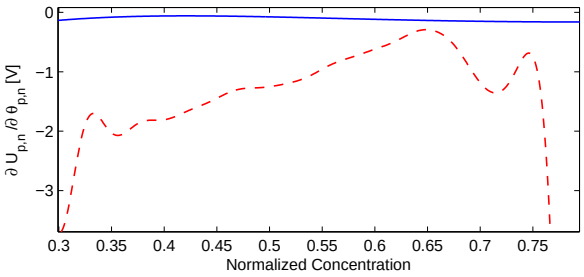

Figure 9 Open circuit potential derivative comparison. Solid blue line is the negative and red dashed line is the positive.

6.2 Minimal Realization and Kalman Filter

The poor observability limitation can be mitigated by establishing a relation between the anode and the cathode average solid concentrations which can be used for the estimation of the negative electrode concentration based on the positive electrode, which can then be observable from the output cell voltage (Di Domenico et al. - CCA, 2008).

Based on manufacturer specification it is possible to define two values for normalized concentration (for both negative and positive values) defined as $\theta_{p,n,100\%}$ and $\theta_{p,n,0\%}$ corresponding respectively to the stoichiometry of a fully charged and a fully discharged battery. It is important to note that $\theta_{n,100\%}$ (or equivalently $\theta_{p,0\%}$) is not equal to 1, because a portion of the lithium is permanently trapped into the anode after the very first charge of the cell and does not flow back to the cathode and viceversa. Common values for $\theta_{p,0\%}$ are $0.7 - 0.9$ depending on cell characteristics and specification about charging and discharging maximum and minimum voltages.

First, let us define the state of charge of the battery immediately available, or critical surface charge, with a good approximation, as linearly varying with θ between the two reference values at 0% and 100%

$$CSC(t) = \frac{\theta_x - \theta_x^{0\%}}{\theta_x^{100\%} - \theta_x^{0\%}}. \tag{34}$$

with $x = p, n$ for the positive and negative electrode. Because the positive open circuit potential function has a higher derivative in respect to the negative, it is best to choose the positive electrode as reference and compute the negative concentration values from the positive ones. With this choice the observability of the system is stronger because the O matrix is less likely to lose rank. Figure 9 shows a comparison between the negative and the positive derivative of the open circuit correlation function. The average difference is around one order of magnitude, with a great value of the positive derivative near to the full charge or the full discharge. Nevertheless, for $\theta_p = 0.65$ (i.e. around 30% SOC) even the positive derivative has a very low value. This reflects the voltage behavior being almost flat for the considered cell around the specified SOC range, and leads to

a weak observability. Finally, equation (34) allows the computation of negative stoichiometry from positive using (34) as

$$\theta_n = \left(\theta_p - \theta_p^{0\%}\right)\left[\frac{\theta_n^{100\%} - \theta_n^{0\%}}{\theta_p^{100\%} - \theta_p^{0\%}}\right] + \theta_n^{0\%} \tag{35}$$

Hence, the state vector can be reduced to

$$x_r = (\bar{c}_{s,p1}, \bar{c}_{s,p2}, ..., \bar{c}_{s,p(M_r-1)})^T, \tag{36}$$

and the dynamical system becomes

$$\dot{x}_r = A_p x_r(t) + B_p u(t), \tag{37}$$

For a linear state-space formulation, the linearized battery voltage results in an output matrix $C = \partial V/\partial x_r$ which is a row matrix with zeros in its first $M_r - 2$ elements and the last non-zero term equal to

$$\frac{\partial V}{\partial \bar{c}_{s,p(M_r-1)}} = \frac{\partial U_p}{\partial \bar{c}_{s,p(M_r-1)}} - \frac{\partial U_n}{\partial \bar{c}_{se,n}} \frac{\partial \bar{c}_{se,n}}{\partial \bar{c}_{s,p(M_r-1)}}. \tag{38}$$

This guarantees a strongly local observability $\forall \bar{c}_{se,p} \neq 0$ (Di Domenico et al. - CCA, 2008; Hermann et al., 1977).

The Kalman filter can now be designed, according to

$$\dot{\hat{x}} = A_p \hat{x} + Bu + K_e(y - \hat{y}) \qquad \hat{y} = V(\hat{x}, u) \tag{39}$$

where $\hat{x}$ and $\hat{y}$ are respectively the estimate state and output, V is the output nonlinear function in (21), A_p, B_p are the matrices describing the dynamical system introduced by (37), C defined using (38) and K_e is the Kalman gain, obtained as follows

$$K_e = PCR_u^{-1} \tag{40}$$

where P is the solution of the Riccati equation

$$\dot{P} = A_p P + PA_p^T - PCR_u^{-1}C^T P + R_x \qquad P(0) = P_0, \tag{41}$$

and R_x and R_u are weight matrices appropriately tuned in order to minimize the quadratic error on battery voltage. A Matlab optimization procedure returned $R_x = 10 \times \mathbf{I}$ (where $\mathbf{I}$ is the identity matrix) and $R_u = 12$. The weak observability discussed above is reflected in a low gain for the Kalman filter in (40) due to the low value of C around 0.3% SOC. This problem can be mitigated choosing an higher value of R_u in this particular region. This leads to a better estimation at the cost of a slower convergence in case of high input dynamics.

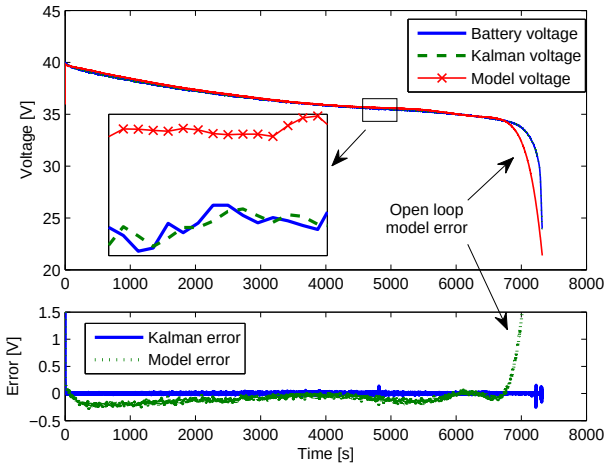

Figure 10 Constant current discharge 3.5 A (0.5 C). Top plot shows the battery voltage output compared with the reduced order model (open loop) and the Kalman filter (closed loop feedback). The bottom plot shows the voltage error committed by the model and by the Kalman filter.

7 Experimental results

In this section the simulation results compared to the experimental data are reported, in order to demonstrate the performance of the Kalman filter. The experiments are similar to the ones used validate the model. The order of the Kalman filter has been chosen equal to 4, in order to ensure a good compromise between accuracy and a realization with a small number of states. Figure 10 shows the filter performance during a constant current discharge of 3.5 A (0.5 C). As is possible to see in the bottom plot, the reduced order model voltage error is lower than 0.5 V almost over the entire discharge process, with a correct initialization of the initial solid concentrations into the electrodes. Nevertheless in the final part, even a very small error in the concentration value leads to a high error in the voltage output, because of the steep behavior of the end-of-discharge voltage characteristic. This could be due to small error in the initial concentration value, differences between the exact battery parameters and the identified parameters, drift of the open loop simulation due to unmodeled phenomena and so on. The Kalman filter instead, thanks to the closed loop feedback regulation is able to follow the battery voltage output with a smaller error along all the discharge and in particular in the final part where the system observability is high. The detail in the top plot highlights the noise rejection property of the filter, that also smooths the voltage noisy signal without losing the real signal dynamics. Figures 11 and 12 show the performances of the Kalman Filter during a pulse discharge compared to both the experimental data from the battery and the open loop model output. The current profile is similar to Figure 6 profile with piecewise constant current demands alternating 10 s rest to 6 A (0.9 C) demand for 5 s. The top plot of Figure 11 shows the comparison between the battery voltage during the pulse and the

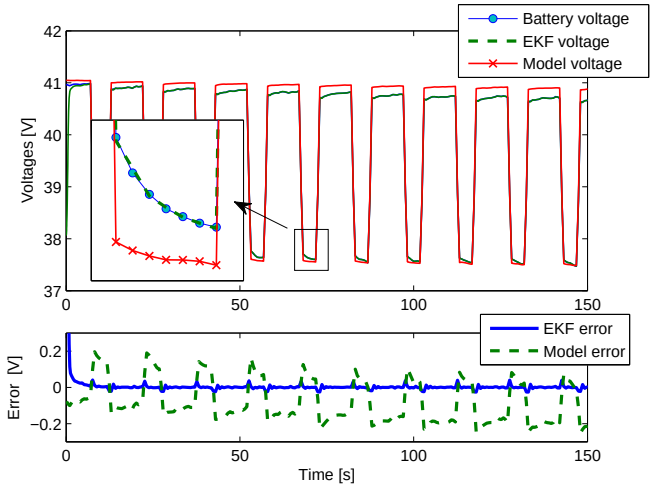

Figure 11 Pulse discharge experiment, beginning of the discharge. The solid blue line with circle marker is the battery measured voltage output, the green dashed line is the EKF voltage output and the red line with the x marker is the open loop model voltage output. The bottom plot shows the error by the EKF and the open loop model.

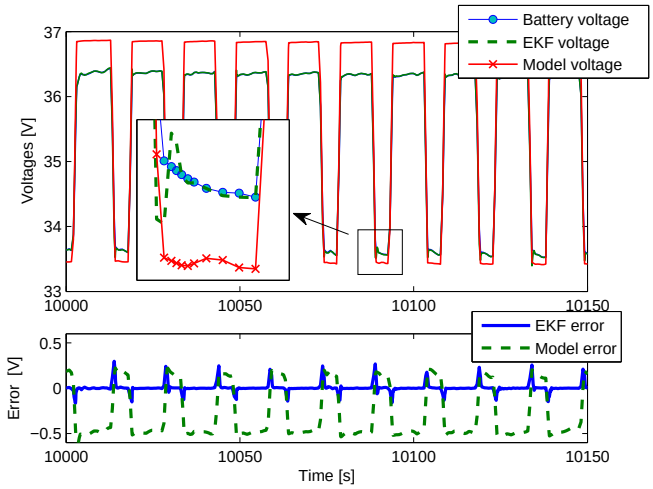

Figure 12 Pulse discharge experiment, close to the end of the discharge. The solid blue line with circle marker is the battery measured voltage output, the green dashed line is the EKF voltage output and the red line with the x marker is the open loop model voltage output. The bottom plot shows the error committed by the EKF and the open loop model.

Kalman filter output along with the open loop model. It it possible to appreciate the higher degree of accuracy of the Kalman filter in respect to the model, even if the latter has been correctly initialized. On the contrary, the convergence property of the Kalman filter eliminates the need of a correct initialization. In fact, the initial concentration values for the Kalman filter are initialized on each experiment on a 50% SOC base, with the filter converging to the correct values in the first 5 seconds, as it is possible to see in the leftmost part of the voltage plot. The zoom shows more detail about the difference in the voltage profile during one of the pulsing current request, where the input dynamics are quite different from the constant current discharge dynamics. The bottom plot of Figure 11 shows the voltage errors of the Kalman filter and the open loop model. The behavior of the open loop model shows clearly that, even if the error is small, the model is unable to replicate the real battery output with more than a certain precision, while the Kalman filter follows closely the experimental data, predicting almost flawlwsly the voltage during both the low and high dynamic part of the profile.

Figure 12 shows the same signals of Figure 11, at the end of the discharge process, close to the low observability part of the model. It is possible to see how, while the EKF shows some errors during the transients (in particular during the current demand fronts as it is possible to notice in the Figure 12 top plot zoom), those errors are quickly recovered. In the contrary, the open loop model error is greater throughout the initial part of the discharge, showed in Figure 11 bottom plot. While the error magnitude is still below the 0.5 V threshold, it is clear that, for this particular profile, the voltage output of the open loop model is by far inaccurate and of no practical interest.

Figure 13 shows the performance of the Kalman filter under noisy input-output condition. The experiment used is the same HPPC profile showed in Figure 7. It is possible to see how the Kalman filter rejects the noise present on the measured battery voltage while still tracking the correct output profile, even in presence of fast input dynamics. On the contrary, the open loop model is subject to the current input noise that gives an equally noisy output. While the open loop error is small compared to the measured battery voltage, there is no filtering action, nor voltage error recovery similar to the Kalman filter predictions.

Figure 14 shows the charge estimation comparison between the SOC based on the critical surface solid concentration (CSOC), the bulk solid concentration (i.e. the whole concentration contained inside the representative spherical particle, or SOC) and the classic coulomb counting (CC), based on the nominal cell capacity value. The experiment used is the 6 A pulse discharge profile used above in the paper. The critical SOC reflects the fast dynamics of the input more than the bulk SOC, while the coulomb counting predicts just a slow decrease of the SOC, due to the pulsing current, neglecting the diffusion/intercalation dynamics captured by the real battery behavior, clearly visible in the cell voltage rising up during the rest periods due to a rebalancing of the surface concentration (and thus of the inner concentration with the diffusion process).

Because the voltage and current signal are noisy, it could be difficult to clearly understand the effective behavior of the concentrations and thus of the calculated SOC. Hence, Figure 15 shows the SOC behavior calculated using a simulated pulse discharge profile. The current demand is a 8 A square wave, with 10 s period and 20% duty cycle. Again the same SOC calculation methods are compared. Since

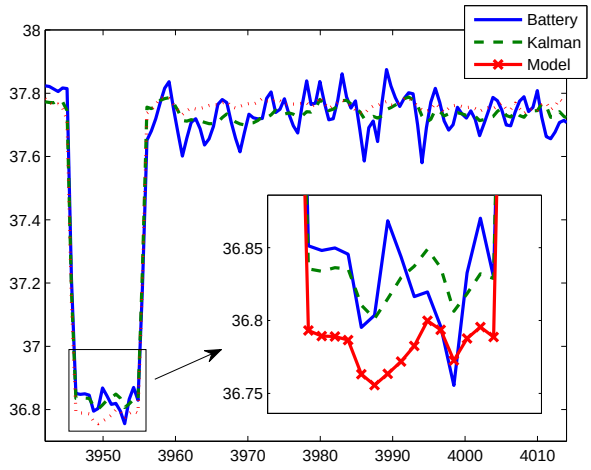

Figure 13 Detail of the HPPC test experiment. The solid blue line is battery measured voltage output, the green dashed line is the Kalman filter voltage output and the red line with the x marker is the open loop model voltage output. The zoom shows the details of the voltages profile, along with the noise filtering action of the EKF in comparison with both the real voltage measurement and the open loop model output.

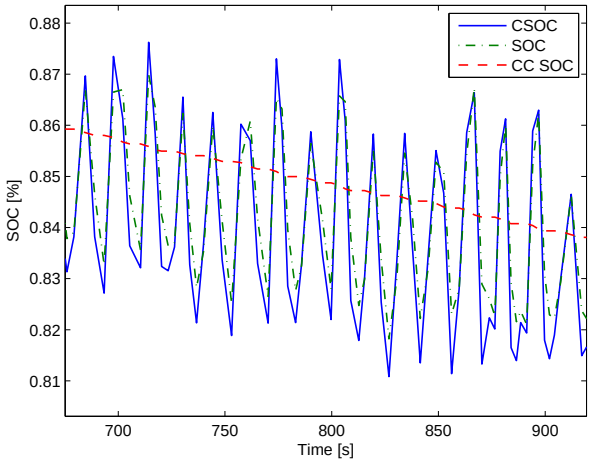

Figure 14 SOC estimation comparison during a pulse discharge experiment. The solid blue line is the EKF critical SOC, the green dotted line is the bulk SOC while the red dashed line is the SOC obtained using the coulomb counting method.

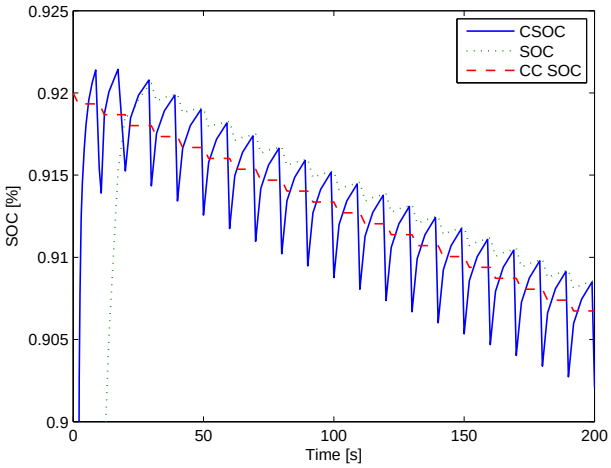

Figure 15 SOC estimation comparison during a simulated pulse discharge experiment. The solid blue line is the EKF critical SOC, the green dotted line is the bulk SOC while the red dashed line is the SOC obtained using the coulomb counting method.

the EKF is always initialized around the 50% value, it is possible to evaluate how the surface concentration converges quickly to the correct value, while the bulk concentration (green dotted line) takes longer because it needs the back propagation effect to reach the inner slices before to converge to the correct values. Again it is possible to see how the simple coulomb counting method fails to catch the rebalancing phenomena that are present instead (even if with a different amplitude) both in the critical and in the bulk SOC estimation. While the mean value of the SOC is practically equal between the critical SOC and the coulomb counting method, the main difference is the istantaneous value of the estimated SOC. The peaks and the valleys in the critical SOC estimation reflect the istantaneous availability of energy due to the presence of a given concentration on the surface of the active material and thus the effective istantaneous available potential at the cell electrodes.

Given a sufficient rest to the cell after a current demand (positive or negative) the value of all the methods has to be equal again, because this value have to reflect the effective amount of energy still present into the cell after the insertion or the extraction. Figure 16 shows the simulation of a 10 s current demand followed by 90 s of rest. It is possible to see how during the rest the EKF SOC estimation (both critical and bulk based) converge to the coulomb counting value, due to the rebalancing of the concentration between the solid and the liquid phase. While this demonstrates that the SOC estimation method proposed is able to give a correct indication of the amount of energy present inside the cell, it has to be noted that the coulomb counting could be used as reference in this case only because the current profile is simulated. In a real environment, the errors due to the noise on the current measure along with unmodeled dynamics of the cell will accumulate making coulomb counting quickly inaccurate. The values estimated by the EKF

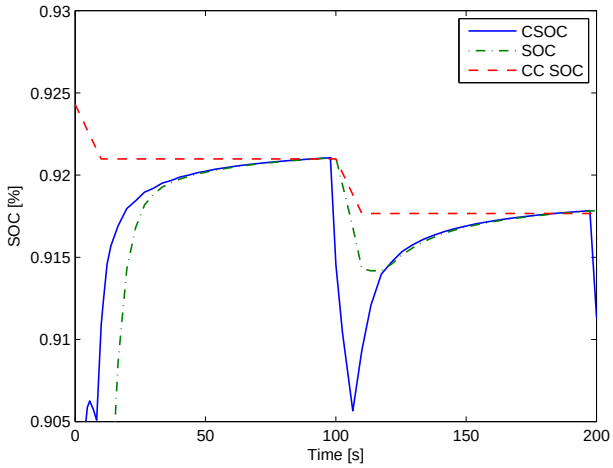

Figure 16 SOC estimation comparison during a 10 s discharge followed by 90 s rest. The solid blue line is the EKF critical SOC, the green dotted line is the bulk SOC while the red dashed line is the SOC obtained using the coulomb counting method.

instead, are always calculated using the voltage feedback in order to estimate the model output error versus the real cell output. This error injection compensates for both model error and small parameter changes from the identified ones.

Finally a robustness analysis has been performed on the Kalman filter in order to verify the robustness of the observer versus variations of the model parameters. For each one of the model parameters, a number of simulations has been performed varying the chosen parameters in order to estimate the resulting output variation. The results of this analysis are listed in Table 3 showing excellent performance in terms of robustness and reliability with respect to the variation of one or more model parameters. For brevity the Table 3 shows just the parameters that lead to a significant SOC estimation variation.

8 Conclusion

An isothermal electrochemical model of the Lithium-ion battery was used to derive an surrogate model coupling the average microscopic solid material concentration with the average values of the chemical potentials, electrolyte concentration and microscopic current density. The surrogate model was identified using experimental data from a 10 cell battery pack. Finally, the SOC estimation was performed using an EKF, showing excellent results in term of voltage convergence indicating good and fast battery SOC estimation and robustness to small battery parameter variations.

Name	Symbol and Value
Max neg. solid concentration *(mol cm^{-3})*	$c_{s,max,n} = 3.175 \times 10^{-2}$
Max pos. solid concentration *(mol cm^{-3})*	$c_{s,max,p} = 2.59 \times 10^{-2}$
Solid phase neg. diffusion coef. *(cm^2 s^{-1})*	$D_{s,n} = 1.27 \times 10^{-12}$
Solid phase pos. diffusion coef. *(cm^2 s^{-1})*	$D_{s,p} = 8.09 \times 10^{-12}$
Neg. active surface area ($cm^2 cm^{-3}$)	$a_{s,n} = 9.655 \times 10^4$
Pos. active surface area ($cm^2 cm^{-3}$)	$a_{s,p} = 2.425 \times 10^4$
Electrode plate Area cm^2	$A = 8000$
Total resistance Ωcm^2	$K_r = 128$
Current density coef.	$k_0 = 1.918 \times 10^3$

Table 1 Parameters identified.

Parameter	Anode	Separator	Cathode
Thickness (cm)	$\delta_n = 0.0005$ (b)	$\delta_{sep} = 0.0002$ (a)	$\delta_p = 0.00364$ (b)
Particle radius R_s (cm)	10×10^{-4} (a)	-	1×10^{-4} (a)
Active material volume frac. ε_s	0.580 (a)	-	0.500 (a)
Electrolyte volume frac. ε_e	0.332 (b)	0.5 (b)	0.330 (b)
Charge transfers coeff. α_a, α_c	0.5,0.5 (b)	-	0.5, 0.5 (b)
Initial stoichiometry x_0,y_0	0.7 (b)	-	0.32 (b)

Table 2 Battery parameters. (a) from battery datasheet, (b) from literature

Parameter	Variation	Absolute error mean
$cs_{max,p}$	-20%	$\bar{e} = 1.1 \times 10^{-3}$
	-10%	$\bar{e} = 4.76 \times 10^{-4}$
	$+10\%$	$\bar{e} = 4.25 \times 10^{-4}$
	$+20\%$	$\bar{e} = 8.10 \times 10^{-3}$
$cs_{max,n}$	-20%	$\bar{e} = 2.1 \times 10^{-3}$
	-10%	$\bar{e} = 9.44 \times 10^{-4}$
	$+10\%$	$\bar{e} = 7.73 \times 10^{-4}$
	$+20\%$	$\bar{e} = 1.4 \times 10^{-3}$
$D_{s,n}$	-20%	$\bar{e} = 7.33 \times 10^{-5}$
	-10%	$\bar{e} = 3.54 \times 10^{-5}$
	$+10\%$	$\bar{e} = 3.33 \times 10^{-5}$
	$+20\%$	$\bar{e} = 6.5 \times 10^{-5}$
$a_{s,p}$	-20%	$\bar{e} = 5.58 \times 10^{-4}$
	-10%	$\bar{e} = 2.48 \times 10^{-4}$
	$+10\%$	$\bar{e} = 2.03 \times 10^{-4}$
	$+20\%$	$\bar{e} = 3.72 \times 10^{-4}$
$a_{s,n}$	-20%	$\bar{e} = 2.12 \times 10^{-3}$
	-10%	$\bar{e} = 9.44 \times 10^{-4}$
	$+10\%$	$\bar{e} = 7.73 \times 10^{-4}$
	$+20\%$	$\bar{e} = 1.41 \times 10^{-3}$
A	-20%	$\bar{e} = 3.57 \times 10^{-3}$
	-10%	$\bar{e} = 1.6 \times 10^{-3}$
	$+10\%$	$\bar{e} = 1.3 \times 10^{-3}$
	$+20\%$	$\bar{e} = 2.39 \times 10^{-3}$
A and $a_{s,n}$	-20%	$\bar{e} = 2.15 \times 10^{-2}$
	-10%	$\bar{e} = 1.1 \times 10^{-2}$
	$+10\%$	$\bar{e} = 1.3 \times 10^{-2}$
	$+20\%$	$\bar{e} = 2.87 \times 10^{-2}$

Table 3 Robustness analysis results.

References

V. Pop, H. Bergveld, P. Notten, P. Regtien, (2005), State-of-the-art of battery state-of-charge determination,*Institute of Physics, Measurement Science and Technology*, Vol. 16 (12), pp.93-110.

A. Schmidt, M. Bitzer, A. Imre, L. Guzzella, (2010), Experiment-driven electrochemical modeling and systematic parameterization for a lithium-ion battery cell, *Journal of Power Sources*, Vol. 195, Issue 15, pp.5071-5080.

Y. Hu, S. Yurkovich, Y. Guezennec, B.J. Yurkovich, (2011), Electro-thermal battery model identification for automotive applications, *Journal of Power Sources*, Vol. 196, Issue 1, pp. 449-457.

G. Plett, (2004), Extended Kalman filtering for battery management systems of LiPB-based HEV battery packs Part 3. State and parameter estimation, *Journal of Power Sources*, Vol. 134, pp.277-292.

K. Smith, (2010) Electrochemical control of Lithium-ion batteries, *IEEE Control Systems Magazine*, Vol. 30, Issue 2, pp.18-25.

N. Chaturvedi, R. Klein, J. Christensen, J. Ahmed, A. Kojic, (2010), Algorithms for Advanced Battery-Management Systems, *IEEE Control Systems Magazine*, Vol.30, Issue 3, pp.49-68.

D. Di Domenico, G. Fiengo, A. Stefanopoulou, (2008), Lithium-ion battery state of charge estimation with a Kalman Filter based on a electrochemical model, *Proceedings of 2008 IEEE Conference on Control Applications*, Vol.1, pp.702-707.

D. Di Domenico, G. Fiengo, A. Stefanopoulou, (2008), Reduced Order Lithium-Ion Battery Electrochemical Model and Extended Kalman Filter State of Charge Estimation, *ASME Journal of Dynamic Systems, Measurement and Control*, Special Issue on Physical System Modeling.

D. Zhang, B. S. Haran, A. Durairajan, R. E. White, Y. Podrazhansky, and B. N. Popov, (2000), Studies on capacity fade of lithium-ion batteries, *Journal of Power Sources*, Vol.91, pp.122-129.

O. Barbarisi, F. Vasca, L. Glielmo, (2006), State of Charge Kalman Filter Estimator for Automotive Batteries, *Control Engineering Practice*, Vol.14, Issue 3, pp.267-275.

F. Codeca, S. Savaresi, G. Rizzoni, (2008), On battery State of Charge estimation: A new mixed algorithm, *IEEE International Conference on Control Applications*, pp.102-107.

K. Smith, C. Rahn, C. Wang; , (2008), Model-based electrochemical estimation of lithium-ion batteries, *IEEE International Conference on Control Applications*, pp.714-719.

K. Smith, C. Rahn, C. Wang; , (2010), Model-Based Electrochemical Estimation and Constraint Management for Pulse Operation of Lithium Ion Batteries, *IEEE Transactions on Control Systems Technology*, Vol.18, Issue 3, pp.654-663.

A.J. Salkind, C. Fennie, P. Singh, T. Atwater, D.E. Reisner, (1999), Determination of State-of-Charge and State-of-Health of Batteries by Fuzzy Logic Methodology, *Journal of Power Sources*, Vol.80, pp.293-300.

C. Chiasserini, R. Rao, (2000), Energy Efficient Battery Management, *Proceedings of Infocom 2000*, pp.396-403.

V. Pop, H. Bergveld, J. Veld, P. Regtien, D. Danilov, P. Notten, (2006), Modeling Battery Behavior for Accurate State-of-Charge Indication, *Journal of Electrochemical Society*, Vol.153, pp.2013-2022.

M. Doyle and T.F. Fuller and J. Newman, (1993), Modeling of Galvanostatic Charge and Discharge of the Lithium/Polymer/Insertion Cell, *Journal of Electrochemical Society*, Vol.140, pp.1526-1533.

P. De Vidts, J. Delgado, R.E. White, (1995), Mathematical Modeling for the Discharge of a Metal Hydride Electrode, *Journal of Electrochemical Society*, Vol.142, pp.4006-4013.

J.W. Weidner, P. Timmerman, (1994),Effect of Proton Diffusion, Electron Conductivity, and Charge-Transfer Resistance on Nickel Hydroxide Discharge Curves, *Journal of Electrochemical Society*, Vol.141, pp.346-351.

M. Chen and G.A. Rincon-Mora, (2006), Accurate Electrical Battery Model Capable of Predicting Runtime and I-V Performance, *IEEE Transactions on Energy Conversion*, Vol.21, pp.504-511.

K. Smith, C.Y. Wang, (2006), Solid-State Diffusion Limitations on Pulse Operation of a Lithium-Ion Cell for Hybrid Electric Vehicles, *Journal of Power Sources*, Vol.161, pp.628-639.

B. Paxton, J. Newmann, (1997), Modeling of nickel metal hydride, *Journal of Electrochemical Society*, Vol.144, pp.3818-3831.

K. Smith, C. Rahn, C. Wang, (2008), Model Order Reduction of 1D Diffusion Systems Via Residue Grouping, *Journal of Dynamic Systems, Measurement, and Control*, Vol.130, Issue 1.

J. Tarascon, D. Guyomard, (1991), Li Metal-Free Rechargeable Batteries Based on Li[sub 1 + x]Mn[sub 2]O[sub 4] Cathodes (0 ¡= x ¡= 1) and Carbon Anodes, *Journal of Electrochemical Society*, Vol.138, pp.2864-2868.

C. Wang, W. Gu, B. Liaw, (1998), Micro-Macroscopic Coupled Modeling of Batteries and Fuel Cells. Part I: Model Development, *Journal of Electrochemical Society*, Vol.145, pp.3407-3417.

W. Gu, C. Wang, (2000), Thermal and Electrochemical Coupled Modeling of a Lithium-Ion Cell, *Proceedings of the ECS*, Vol.99, pp.748-762.

C. Wang, W. Gu, B. Liaw, (1998), Micro-Macroscopic Coupled Modeling of Batteries and Fuel Cells. Part II: Application to Ni-Cd and Ni-MH Cells, *Journal of Electrochemical Society*, Vol.145, pp.3418-3427.

T. Fuller, M. Doyle, J. Newman, (1994), Simulation and Optimization of the Dual Lithium Ion Insertion Cell, *Journal of Electrochemical Society*, Vol.141, pp.1-10.

M. Doyle, J. Newman, A. Gozdz, C. Schmutz, J. Tarascon, (1996), Comparison of Modeling Predictions with Experimental Data from Plastic Lithium Ion Cells, *Journal of Electrochemical Society*, Vol.143, pp.1890-1903.

T. Fuller, M. Doyle, J. Newman, (1994), Relaxation phenomena in lithium-ion insertion cells, *Journal of Electrochemical Society*, Vol.141, pp.982-990.

M. Doyle, Y. Fuentes, (2003), Computer Simulations of a Lithium-Ion Polymer Battery and Implications for Higher Capacity Next-Generation Battery Designs, *Journal of Electrochemical Society*, Vol.150, pp.706-713.

U.S. Department of Energy, (2003), FreedomCAR battery Test Manual For Power-Assist Hybrid Elecric Veicles, *DOE/ID-11069*.

R. Hermann, A. Krener, (1977), Nonlinear controllability and observability, *IEEE Transactions on Automatic Control*, Vol.22, pp.728-740.

A. Schmidt, M. Bitzer, A. Imre, L. Guzzella, (2010), Experiment-driven electrochemical modeling and systematic parameterization for a lithium-ion battery cell, *Journal of Power Sources*, Vol.195, pp.5071-5080.